

The PICS Project

I. The impact of metallicity and helium abundance on the bright end of the planetary nebula luminosity function

Lucas M. Valenzuela¹, Marcelo M. Miller Bertolami^{2,3}, Rhea-Silvia Remus¹, and Roberto H. Méndez⁴

¹ Universitäts-Sternwarte, Fakultät für Physik, Ludwig-Maximilians-Universität München, Scheinerstr. 1, 81679 München, Germany
e-mail: lval@usm.lmu.de

² Instituto de Astrofísica de La Plata, UNLP-CONICET, La Plata, Paseo del Bosque s/n, B1900FWA, Argentina

³ Facultad de Ciencias Astronómicas y Geofísicas, UNLP, La Plata, Paseo del Bosque s/n, B1900FWA, Argentina

⁴ Institute for Astronomy, University of Hawaii, 2680 Woodlawn Drive, Honolulu, HI 96822, USA

Received XX Month, 20XX / Accepted XX Month, 20XX

ABSTRACT

Context. Planetary nebulae (PNe) and their luminosity function (PNLF) in galaxies have been used as a cosmic distance indicator for decades, yet a fundamental understanding is still lacking to explain the universality of the PNLF among different galaxies. Models for the PNLF have so far generally assumed near-solar metallicities and employed artificial stellar populations.

Aims. In this work, we investigate how metallicity and helium abundances affect the resulting PNe and PNLF, as well as the importance of the initial-to-final mass relation (IFMR), to resolve the tension between PNLF observations and previous models.

Methods. We introduce PICS (PNe In Cosmological Simulations), a PN model framework that takes into account the stellar metallicity and is applicable to realistic stellar populations obtained from both cosmological simulations and observations. The framework combines current stellar evolution models with post-AGB tracks and PN models to obtain the PNe from the parent stellar population.

Results. We find that the metallicity plays an important role for the resulting PNe: old metal-rich populations can harbor much brighter PNe than old metal-poor populations. In addition, we show that the helium abundance is a vital ingredient at high metallicities and explore the impact on the PNLF of a possible saturation of the helium content at higher metallicities. We present PNLF grids for different stellar ages and metallicities, where the observed PNLF bright end can be reached even for old stellar populations of 10 Gyr at high metallicities. Finally, we find that the PNLFs of old stellar populations are extremely sensitive to the IFMR, potentially allowing for the production of bright PNe.

Conclusions. With PICS, we have laid the groundwork for studying how models and assumptions relevant to PNe affect the PNe and PNLF. Two of the central ingredients for this are the metallicity and helium abundance. Future applications of PICS include self-consistent modeling of PNe in a cosmological framework to explain the origin of the universality of the PNLF bright-end cutoff and use it as a diagnostic tool for galaxy formation.

Key words. Galaxies: distances and redshifts – Galaxies: stellar content – planetary nebulae: general – Stars: AGB and post-AGB – Stars: evolution – Stars: luminosity function, mass function

1. Introduction

For more than 30 years, planetary nebulae (PNe) have been used as distance indicators in the cosmic distance ladder through the luminosity function of their [O III] $\lambda 5007$ magnitude in extragalactic systems, referred to as the planetary nebula luminosity function (PNLF) (Jacoby 1989). Because it was observed that the PNLF has a universal bright end cutoff magnitude independent of the galaxy morphology, it has been found to work well as a distance indicator (e.g., Ciardullo et al. 1989; Jacoby et al. 1990; Rekola et al. 2005). Despite the wide usage, the underlying physics of the universality of the PNLF has remained a mystery in particular due to the question how old elliptical galaxies should be able to host any PNe as bright as the ones observed at the magnitude cutoff (Ciardullo 2012). The argument for this has been that old stars at the main-sequence turnoff are too low in mass to produce such high emission in [O III]. The PNLF has been successfully used as a distance indicator for galaxies at distances of up to 10–15 Mpc, but has been limited to within 20 Mpc because of the limitations of narrowband filter imaging (Roth et al. 2021).

In the past ten years, there have been two significant advances on the modeling and observational sides. With respect to modeling, Miller Bertolami (2016) computed updated post-asymptotic giant branch (AGB) tracks of potential PN central stars. Those tracks were the first major update to the formerly computed stellar tracks from over 30 years ago (e.g., Schönberner 1983; Vassiliadis & Wood 1994; Blöcker 1995). These new tracks featured a much faster post-AGB evolution with timescales shorter by a factor of three to ten and with brighter post-AGB stars. These led to several PN models being developed in recent years with a particular focus on improving the understanding of the universal bright end of the PNLF. Overall, the brighter post-AGB evolution has slightly diminished the large discrepancy between the observed bright PNe in old stellar populations and the models (e.g., Gesicki et al. 2018; Valenzuela et al. 2019). Further models have been developed with alternative attempts of explaining the bright end of the PNLF, including accreting white dwarfs (WDs; e.g., Soker 2006; Souropanis et al. 2023) and WD mergers (e.g., Ciardullo et al. 2005; Yao & Quataert 2023).

On the observational side, the integral field unit (IFU) measurements with the instrument MUSE have made it possible to obtain the full spectra for each individual pixel, thereby making the detection of PNe and the removal of contaminants possible without follow-up measurements. This improves on former methods like the PN Spectrograph (PN.S; Douglas et al. 2002) and extended PN.S (ePN.S; Pulsoni et al. 2018). Using MUSE, several works have analyzed extragalactic PN populations, getting better data for previously studied objects or investigating new systems (e.g., Kreckel et al. 2017; Spriggs et al. 2020; Roth et al. 2021; Scheuermann et al. 2022; Soemitro et al. 2023; Jacoby et al. 2024). Furthermore, the high resolution of MUSE is expected to make it possible to reach distances of up to 40 Mpc, more than twice as far compared to previous limits (Roth et al. 2021).

To establish a theoretical foundation for the PNLF and the usefulness of its bright end as a distance indicator, numerous approaches have been taken throughout the years to explain the properties of the PNLF. Some authors have created models for the entire population of PNe based on mock stellar populations (e.g., Méndez et al. 1993; Méndez & Soffner 1997; Schönberner et al. 2007; Valenzuela et al. 2019), others have employed analytic properties of the PNLF (e.g., Rodríguez-González et al. 2015). In contrast, the majority of studies have focused on the bright end specifically, that is the maximum brightnesses that are achievable by PNe of certain stellar populations (e.g., Dopita et al. 1992; Marigo et al. 2004; Gesicki et al. 2018; Souropanis et al. 2023; Yao & Quataert 2023). One of the findings from theory and observations has been that there should be a slight dependence of the PNLF bright end on metallicity, where the bright end becomes fainter for very metal-poor systems (e.g., Ciardullo & Jacoby 1992; Dopita et al. 1992; Ciardullo et al. 2002; Ciardullo 2010). However, the theoretical expectation that older stellar populations would produce PNLFs with their bright end being significantly dimmer is not observed (e.g., Marigo et al. 2004; Ciardullo 2012, stating that the PNLF bright end should already be more than 4 magnitudes dimmer for ages of 10 Gyr).

Not only the bright end of the PNLF has drawn attention, but also the faint shape of the PNLF: the general shape was introduced by Ciardullo et al. (1989) as an exponential cutoff function with a parameter describing the slope on the faint side. This slope has been predicted to encode clues about the star formation history (e.g., Ciardullo 2010; Longobardi et al. 2013; Hartke et al. 2017) and has been investigated in particular for the different substructures in the outskirts of M 31 (Bhattacharya et al. 2021). For this, Bhattacharya et al. (2021) also used the approach of fitting a superposition of two modes of the PNLF following Rodríguez-González et al. (2015). A further interesting feature that has been observed in the faint part of the PNLF is a dip for galaxies with recent star formation, that is a lower abundance of PNe at an intermediate magnitude (e.g., Jacoby & De Marco 2002; Reid & Parker 2010; Soemitro et al. 2023). Even some models have been able to find such a dip in the PNLF for younger stellar populations (e.g., Méndez et al. 2008; Valenzuela et al. 2019).

With the multitude of observations and modeling approaches, the continual lack of fundamental understanding concerning the PNLF suggests that some of the previously employed assumptions are insufficient to address the problem at whole. Indeed there are two central assumptions that have been commonly made in PN models over the years that do not represent realistic stellar populations as they are found in actual galaxies: First, models have mostly only been applied to stars with fixed metallicities around the solar metallicity with respect to their main sequence (MS) and post-MS lifetimes, the initial-to-final mass relation (IFMR),

or the post-AGB evolution (e.g., Gesicki et al. 2018; Valenzuela et al. 2019; Souropanis et al. 2023), despite the findings that metallicity does in fact play a role for the brightness of PNe. Furthermore, even stellar evolution models employ many recipes based on measurements of the Sun and assume abundances based on the Milky Way (e.g., Miller Bertolami 2016), where the helium abundance has oftentimes been assumed to scale linearly with metallicity, though this has been put into question recently (e.g., Clontz et al. 2024). Second, the studies that have attempted to model the entire PN population have set up artificial mock stellar populations with the goal of mimicking selected real galaxies (e.g., Méndez & Soffner 1997; Valenzuela et al. 2019), but again relying on observations in the Milky Way, specifically the WD mass distribution. These models therefore fall short of accurately representing the large diversity of galaxies and star formation histories, which can strongly vary depending on intrinsic factors and the cosmological environment.

To overcome these limitations of current PN models, we introduce PICS (PNe In Cosmological Simulations), a modular framework for modeling PNe within any given stellar population, taking into account properties such as mass, age, metallicity, and the initial mass function (IMF). In the era of hydrodynamical cosmological simulations, a new approach is further possible: realistic stellar populations with self-consistent properties in the cosmological context can be directly obtained for a large variety of galaxies from such simulations. With PICS we present the very first method for bringing PNe into cosmological simulations and simultaneously improve on previous PN models by fully considering the metallicity and specific abundances beyond solar values. Finally, the modular nature of the framework allows for controlled testing of different parameters and individual models, which we will also demonstrate in this paper.

In Sect. 2, we present the PICS model structure and the implementation of the fiducial model, including the metallicity dependence on the individual modules. By combining some of the modules, we then show how the metallicity and helium abundances affect the stellar evolution relevant for PNe in Sect. 3. In Sect. 4, we present grids of PNLFs resulting from different pairs of ages and metallicities and from varying the IFMR – these are the building blocks for any real PNLF. Finally, we summarize the results and conclude in Sect. 5.

2. Model

In the following, we describe the building blocks of the PICS model. Its target is to take a given single stellar population (SSP) parameterized by a set of properties and determine the contained PN population. The obtained PN properties in particular include the magnitude of the emitted [O III] line, as it is the primary intrinsic observable quantity of an extragalactic PN. This procedure will make it possible to apply PICS to both observed galaxy star formation histories discretized by SSPs and to the stellar particles extracted from cosmological simulations (Soemitro et al. in prep.; Valenzuela et al. in prep.). The end result is then a full population of PNe for an entire system like a galaxy or galaxy cluster.

The model is designed to be modular, meaning that the individual parts described in the following can be replaced with different underlying models, and the selection of models will also be continuously expanded in future versions. In this work, we present the fiducial model and some alternative relations for the IFMR and how they affect the PNLF. The source code and more information on using the model are made available on-

line.¹ A summary of the model functionality is presented in the proceedings by Valenzuela et al. (2024).

2.1. Single stellar population properties

An SSP represents the population of stars having formed from a gas cloud where all the member stars share the same underlying age and chemical composition. The distribution of stellar masses within the SSP is given by an IMF. In its simplest form, the input SSP properties need to include its total mass, an IMF, and its age. The age is needed to determine the initial mass range of stars now residing within the PN phase after having left the AGB track. The IMF is used to determine the fraction of stars that are within that initial mass range, and the total mass sets the absolute number of those stars. In addition to these properties, further quantities significantly influence the processes relevant for stellar evolution and PNe: in particular, we show in this work that the stellar metallicity is a vital parameter that affects the duration of stellar evolution on the MS and post-MS. In the future, individual abundances like helium or α -element abundances will also be added as quantities that are taken into account.

In this work, each SSP is parameterized with the following quantities:

- IMF, for this work we only consider that by Chabrier (2003)
- total mass M_{tot} of the SSP
- age t , that is the time since the formation of the SSP stars
- metallicity Z , in this work quantified as the initial metal mass fraction: $Z = M_{\text{met,init}}/M_{\text{tot,init}}$. As a point of reference, the solar metallicity lies between $Z = 0.01$ and 0.02 (e.g., Asplund et al. 2009; Caffau et al. 2011; von Steiger & Zurbuchen 2016).

2.2. Stellar lifetime function

In the context of PN modeling, we define the stellar lifetime as the time from the birth of a star until it leaves the AGB phase and enters the post-AGB phase, during which a star can become a PN. It therefore roughly corresponds to the combined MS and post-MS lifetimes from other works (e.g., Renzini 1981; Renzini & Buzzoni 1986; Padovani & Matteucci 1993). The purpose of this module in PICS is to return the initial stellar mass of the stars that now are passing through the PN phase after the age t . Due to the short-lived nature of the PN phase (assumed as 30 000 yr here), the time spent after the departure from the AGB phase is negligible for the initial mass of the star. Then, disregarding binary interactions, we can assume that all PNe in a single stellar population are descendants of stars with the same initial mass.

For this work we took the lifetimes of the stellar evolution simulations from Miller Bertolami (2016), given in their tab. 2. For each of their considered metallicities ($Z = 0.0001, 0.001, 0.01, \text{ and } 0.02$) and initial masses (ranging from $M_{\text{init}} = 0.8\text{--}4.0 M_{\odot}$, depending on the metallicity), we added up all the stated lifetimes: MS, red giant branch (RGB), core He-burning, early AGB, and thermally pulsing AGB (TP-AGB) phases as an M-type and carbon star. Taking these lifetimes and the initial masses from Miller Bertolami (2016), we fit a double power law for each of the four metallicities ($Z = 0.0001, 0.001, 0.01, \text{ and } 0.02$) by fitting a power law to the lower masses up to and including $1.5 M_{\odot}$ and a power law to the higher masses starting at $1.5 M_{\odot}$ (i.e., with one value in common). Table 1 shows the fitting parameters for the free parameters of

$$t/\text{Gyr} = a \times (M_{\text{init}}/M_{\odot})^k \quad (1)$$

Table 1. The lifetime function double power law fit parameters for the low ($\leq 1.5 M_{\odot}$) and high initial masses ($\geq 1.5 M_{\odot}$) at the given metallicities Z from Miller Bertolami (2016), parameterized as $t/\text{Gyr} = a \times (M_{\text{init}}/M_{\odot})^k$.

Z	a_{low}	k_{low}	a_{high}	k_{high}
0.0001	11.80	−3.58	7.98	−2.55
0.001	9.72	−3.52	6.54	−2.45
0.01	6.41	−3.45	4.64	−2.45
0.02	5.95	−3.40	4.75	−2.65

for the low and high masses at the four metallicities, which lead to very good descriptions of the original data points, even in logarithmic space.

These fits only correspond to the four discrete metallicities from Miller Bertolami (2016). To obtain a continuous representation of the lifetime function across metallicities, we found the following relations to describe the change of the four double power law parameters with metallicity²:

$$a_{\text{low}} = 78.27 \times Z^{0.649} + 5.67, \quad (2)$$

$$a_{\text{high}} = 107.5 \times Z^{0.880} + 4.58, \quad (3)$$

$$k_{\text{low}} = -0.943 \times Z^{0.400} - 3.38, \quad (4)$$

$$k_{\text{high}} = -3.29 - 0.654 \times (\log Z) - 0.124 \times (\log Z)^2. \quad (5)$$

The lifetime is then determined as the maximum between t_{low} and t_{high} computed from the respective power law parameters obtained from the stated relations. The lifetime function is shown for the original and some selected further metallicities in Fig. 1, showing the continuous nature of the here derived expression. In Sect. 3, we present how the extrapolation of this relation to higher metallicities compares to detailed evolutionary models computed at such higher metallicities.

The obtained lifetime functions at the four original metallicities (Eqs. 2 to 5) as well as at intermediate and one lower metallicity ($Z = 0.00001$) are shown in Fig. 1 as lines, colored by metallicity. The circular points indicate the values obtained from tab. 2 of Miller Bertolami (2016) and lie directly on the respective thick solid functional lines. The thin lines, which are at interpolated and lower metallicities, lie between the thick lines, just as they should. We therefore conclude that our determined analytical lifetime function is suitable for metallicities of at least $Z = 0.00001\text{--}0.02$.

While other PN studies have generally implicitly or explicitly assumed a fixed metallicity for their underlying mock stellar populations, oftentimes $Z = 0.01$ or $Z = 0.02$ (e.g., Gesicki et al. 2018; Souropanis et al. 2023; Valenzuela et al. 2019), Fig. 1 shows that the metallicity plays a very significant role for stars of any age. For a fixed stellar age, varying the metallicity from low values of $Z = 0.0001$ to $Z = 0.02$ results in a change of more than $M_{\text{init}} = 0.2 M_{\odot}$. In contrast, large absolute changes of stellar age for $t \lesssim 5$ Gyr only slightly affect the initial mass, which becomes relevant towards lower masses as the mass approaches the minimum viable mass for PNe to form, however. For old elliptical galaxies the metallicities tend to be high (e.g., Li et al. 2018), which means that especially for those types of galaxies it is important to take into account the actual underlying stellar metallicity. The implications of a higher metallicity are the following: at a fixed stellar age, more metal-rich stars now passing through the PN phase are more massive than metal-poor stars that are PNe because more

² See the implementation in the source code on GitHub for the exact values with more significant digits.

¹ <https://lucasvalenzuela.de/PICS/>

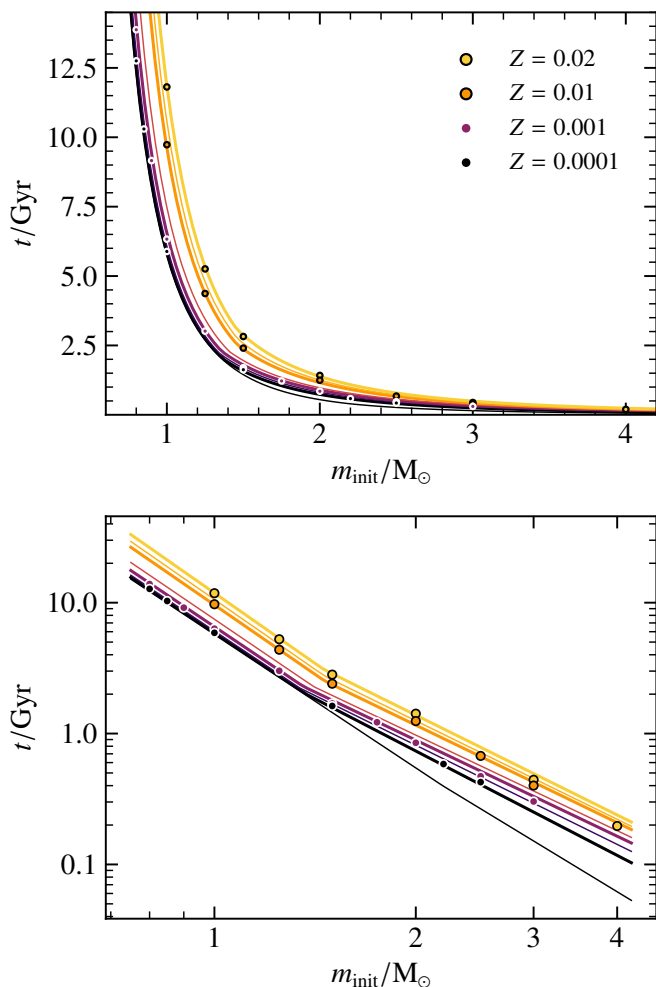


Fig. 1. Lifetime function of stars until they reach the post-AGB phase as a function of their initial mass. *Top:* Linear axes. *Bottom:* Logarithmic axes, which makes it easier to distinguish the individual lines and data points. The points are from the models by Miller Bertolami (2016), and the lines are the fit relations to those data points. The thick lines are at the same metallicities as the ones from the original models ($Z = 0.0001, 0.001, 0.01, \text{ and } 0.02$) and the thin lines are at $Z = 0.00001, 0.0003, 0.003, 0.014$, where the latter three values are the logarithmic midpoints of the original metallicities.

metal-rich stars evolve more slowly at a fixed stellar mass. This leads to more massive central stars with higher temperatures and luminosities, thus giving rise to brighter PNe, which is a possible way of populating the bright side of the PNLF with PNe from older stellar populations.

2.3. Initial-to-final mass relation

Having obtained the initial mass of stars that are now PNe, the IFMR is next used to determine the final mass based on the initial mass and metallicity of the star, that is how massive the central star of the PN is. This relation has been mainly investigated through WD stars in star clusters in the solar neighborhood (e.g., Cummings et al. 2018).

For the fiducial model, we create a metallicity-dependent IFMR based on the values obtained from the models of Miller Bertolami (2016), which includes the four metallicities $Z = 0.0001, 0.001, 0.01, \text{ and } 0.02$, just as for the lifetime function (Sect. 2.2). To sample more data points between the simu-

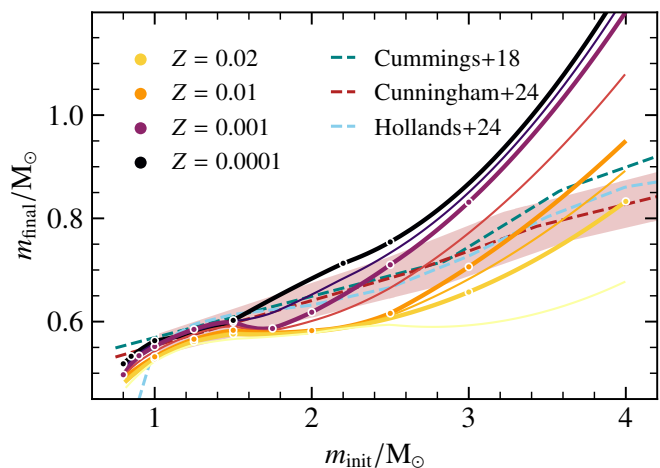


Fig. 2. Initial-to-final mass relation of stars. The points are from the models by Miller Bertolami (2016), and the lines in the corresponding colors are the fit relations to those data points. The thick lines are at the same metallicities as the ones from the original models ($Z = 0.0001, 0.001, 0.01, \text{ and } 0.02$) and the thin lines are at $Z = 0.00001, 0.0003, 0.003, 0.014, 0.05$, where the middle three values are the logarithmic midpoints of the original metallicities. Additionally, three observationally based IFMRs from nearby WD measurements at solar metallicity are shown from Cummings et al. (2018), Cunningham et al. (2024), and Hollands et al. (2024), as well as the 1σ uncertainty band of Cunningham et al. (2024).

lated pairs of initial and final mass values at each metallicity, a forward-looking quadratic interpolation (Bhagavan et al. 2024) is used. Then, a 2D linear interpolation is applied between the four logarithmic metallicities to the more finely sampled values, which is the resulting metallicity-dependent IFMR. This IFMR can be applied in two extrapolation modes: for metallicities outside of the range of $Z = 0.0001$ – 0.02 , the values at the respective bounding metallicity can be used as a constant beyond that value, or the linear fit can be extrapolated beyond the original metallicity range. In Fig. 2, we show the resulting IFMR with extrapolated values at the same metallicities as shown for the lifetime function in Fig. 1, plus the higher metallicity of $Z = 0.05$. The colored dots show the original data points from table 2 of Miller Bertolami (2016), between which the interpolation took place.

The dependence on metallicity of the IFMR shows that more metal-rich stars at a fixed initial mass end up having lower final masses than metal-poor stars. As more massive stars are hotter and more luminous in the post-AGB phase and thus lead to brighter PNe, this counteracts the effect that metallicity has on the lifetime function, which leads to stars with higher initial masses entering the PN phase.

It is worth noting that the metallicity dependence of the IFMR of the models of Miller Bertolami (2016) is a consequence of the adopted winds. The metallicity dependence of cold winds is still poorly understood, in particular in the first RGB phase. The resulting theoretical IFMRs should therefore be taken as educated guesses. Most reliable IFMRs come from semi-empirical studies of star clusters in the solar neighborhood, which are only available for near-solar metallicities, however.

As the IFMR in general and also its metallicity dependence are still poorly understood, it is important to better understand the dependence of the resulting PNe in a given SSP on the used IFMR. For this, we additionally consider three IFMRs derived from observed WDs in the Milky Way: Cummings et al. (2018) determined their IFMR from 80 WDs located in 13 star clusters,

Cunningham et al. (2024) studied 40 WDs from Gaia data within 40 pc of the Sun, and Hollands et al. (2024) studied 90 WD binaries from Gaia data with distances of up to 250 pc. All three of these IFMRs correspond to near-solar metallicities. We also show IFMRs from the three studies in Fig. 2, where we use the adopted MIST-based IFMR of Cummings et al. (2018) and linearly extrapolate all three IFMRs down to lower initial masses, as Cunningham et al. (2024) and Hollands et al. (2024) only fit their IFMRs down to $1 M_{\odot}$, and Cummings et al. (2018) to $0.83 M_{\odot}$. The uncertainties of these IFMRs are on the order of $\sigma_{M_{\text{final}}} \approx 0.025 M_{\odot}$, for which we also show the uncertainty region of Cunningham et al. (2024). Further, the systematic uncertainties are on the order of $0.1 M_{\odot}$, as seen by using different underlying stellar evolution model is employed (Cummings et al. 2018). While these relations are all monotonic, we note that it is still debated whether this is the case or if there is a dip around $m_{\text{init}} \approx 1.5\text{--}2 M_{\odot}$ (e.g., Marigo et al. 2020) due to the large uncertainties.

Overall, there is a general agreement on what the IFMR looks like within the measurement uncertainties and their large systematics, where the theoretical metallicity-dependent IFMR from Miller Bertolami (2016) predicts overall lower final masses at solar metallicity than the observationally based IFMRs, especially at final masses of $m_{\text{init}} \approx 1.5\text{--}3 M_{\odot}$ around the potential dip. Still, the small differences in final mass can lead to significant changes in the resulting PN properties, especially moving towards final masses below $0.6 M_{\odot}$. In Sect. 4, we investigate how the different IFMRs impact the resulting PN population with respect to their PNLF.

2.4. Post-AGB stellar evolution tracks

With the final mass of the star in question, the evolving properties of the central star can be obtained from post-AGB stellar evolution tracks. In particular, the luminosity L and effective temperature T_{eff} can be directly obtained with the tracks in the Hertzsprung-Russell diagram, given the final mass and an identifying time. For PICS, we assume the lifetime of a PN can be up to 30 000 yr (Valenzuela et al. 2019). For a given central star, the time since leaving the post-AGB phase is therefore randomly drawn from a uniform distribution between 0 and 30 000 yr, as the timescale is negligible compared to the timescale of the MS and post-MS.

In this work, we use the post-AGB tracks of the H-burning stars from Miller Bertolami (2016) and interpolate them to obtain the central star luminosity and effective temperature as a function of metallicity, final mass, and the post-AGB age (see Appendix A for details on the interpolation). Following the approach of Valenzuela et al. (2019), we take the post-AGB age to be the time since the temperature reached a value of $T_{\text{eff}} = 25\,000$ K ($\log T_{\text{eff}}/\text{K} \approx 4.40$). The interpolated post-AGB tracks at two final masses of $m_{\text{final}} = 0.55$ and $0.58 M_{\odot}$ (of which only the former mass was explicitly computed by Miller Bertolami 2016) for a range of different metallicities can be seen in Fig. 3. Clearly, the interpolations successfully produce intermedial values, in particular between the originally simulated metallicities. For metallicities outside of the range between $Z = 0.0001$ and 0.02 , we simply use the respective tracks at $Z = 0.0001$ or $Z = 0.02$.

Additionally, it can here be seen that more metal-poor stars at a fixed final mass have a higher luminosity and can reach higher temperatures than metal-rich stars, as was also shown by Miller Bertolami (2016). Like the metallicity-dependent IFMR from Miller Bertolami (2016) presented in Sect. 2.3, this counteracts the effect the lifetime function has that one would expect more metal-rich stars to host brighter PNe, as well as the lower

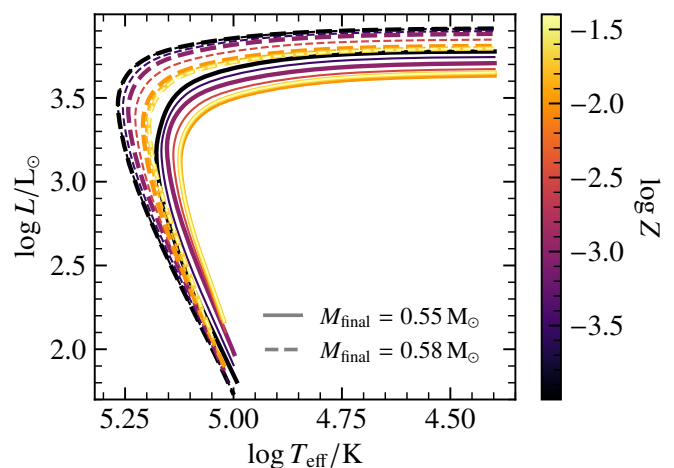


Fig. 3. Post-AGB tracks in the Hertzsprung-Russell diagram of stars at two final masses $M_{\text{final}} = 0.55 M_{\odot}$ and $0.58 M_{\odot}$ for a range of metallicities. The tracks are interpolated between the data tables from Miller Bertolami (2016). The metallicity colorbar corresponds to the same coloring as found in Figs. 1 and 2. The thick lines are at the same metallicities as the ones from the original models ($Z = 0.0001, 0.001, 0.01, \text{ and } 0.02$) and the thin lines are at $Z = 0.00001, 0.0003, 0.003, 0.014, 0.05$, where the middle three values are the logarithmic midpoints of the original metallicities.

number of oxygen atoms in the nebula, which is also expected to limit the brightness of the [O III] line. The dependence of the maximum luminosity and effective temperature of a star on its metallicity and age is therefore not trivial.

2.5. Planetary nebula model

The central star properties can finally be used to infer the PN emissions. Particularly, the [O III] intensity is of great importance for studies of extragalactic PNe. Additionally, properties such as the H β intensity may be of further relevance and has been studied for extragalactic PN populations as well (e.g., Reid & Parker 2010).

In this work we use the PN model from Valenzuela et al. (2019). To our knowledge it is the only current PN model that not only addresses the brightest PNe at the bright end of the PNLF, but can also be used to produce dim PNe that are consistent with observations, while being applicable to large numbers of central stars without exceedingly high computational cost. The model computes the maximum total intensity of H β emission assuming optical thickness, $I(\text{H}\beta)$, based on the luminosity of the central star luminosity and its blackbody radiation given by the effective temperature. Next, the ratios between $I(\text{H}\beta)$ and the intensity of the [O III] emission line $I(5007)$ that have been empirically obtained $I(5007)$ for a given PN. This ratio is drawn from a Gaussian distribution and is modified by some physically motivated prescriptions based on stellar mass and temperature. For the details on this prescription, refer to Valenzuela et al. (2019).

Finally, an absorbing factor μ is applied to the intensities to account for ionizing stellar photons that are not absorbed by the nebula. The absorbing factor is equivalent to the fraction of ionizing photons that are actually absorbed and is simply multiplied with the previously obtained intensity to get the observed value of $I(5007)$. The absorbing factor for a given star is drawn

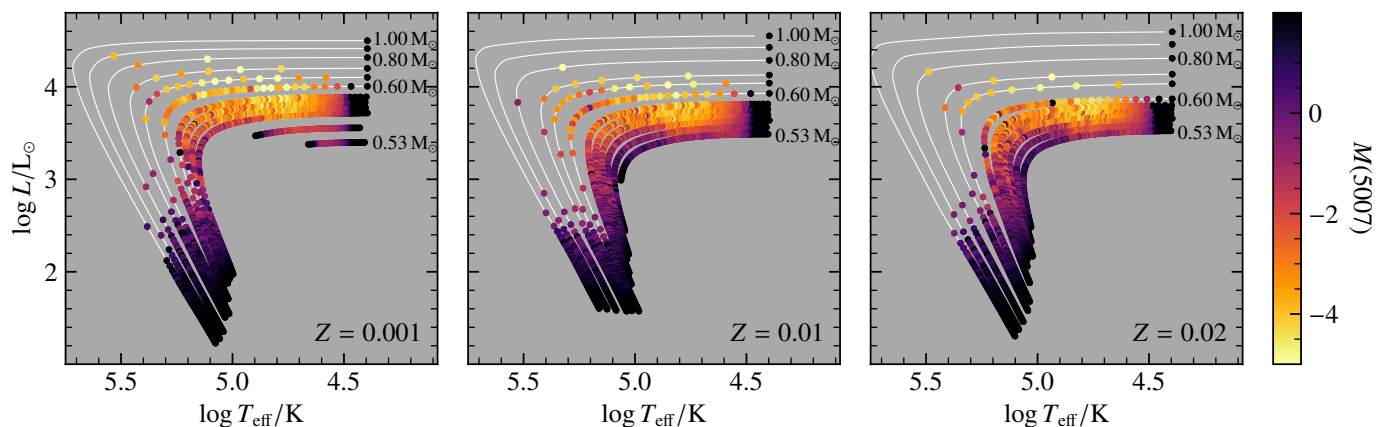


Fig. 4. Post-AGB tracks in the Hertzsprung-Russell diagram of stars at metallicities $Z = 0.001$, 0.01 , and 0.02 (left, middle, and right, respectively), colored by the $\lambda 5007$ magnitude. The tracks are shown for stars at different final masses $M_{\text{final}} = 0.53, 0.54, 0.55, 0.56, 0.57, 0.58, 0.60, 0.65, 0.70, 0.80, 0.90$, and $1.00 M_{\odot}$. For each final mass, stars at 600 evenly spaced post-AGB ages between 0 and 30 000 yr are plotted. The white lines indicate the tracks for the selected central star masses.

randomly because of possible asymmetries in the nebula that can lead to a leakage of ionizing photons (for more details see Méndez & Soffner 1997; Valenzuela et al. 2019). Additionally, its maximally allowed value is decreased over the lifetime of the PN, which accounts for the nebula dissipating over time. One aspect that is not included in the model is the internal dust extinction, which becomes more important for younger stars (e.g., Jacoby & Ciardullo in prep.), which means in general for higher stellar masses. Such a model is planned to be included in the future. As it only is of relevance for younger, more massive PNe, it is mostly important for lowering the brightness at the bright end of the PNLf, meaning that this plays a much smaller role for the dimmer, lower-mass PNe relevant for old galaxy populations.

In Fig. 4 we show the post-AGB tracks in the Hertzsprung-Russell diagram of stars with certain final central star masses at metallicities of $Z = 0.001$, 0.01 , and 0.02 . The data points show individual PNe at evenly spaced ages between 0 and 30 000 yr starting from the given track reaching $T_{\text{eff}} = 25\,000$ K. The PNe are colored according to their [O III] $\lambda 5007$ absolute magnitude, $M(5007) = -2.5 \log I(5007) - 13.74$ with $I(5007)$ being the intensity seen 10 pc away, as defined by Jacoby (1989). According to the model, the brightest PNe for a given central star mass are located on the rising temperature track, after which the intensity of the [O III] line decreases again due to the dispersion of the nebula over time and the eventual drop of the star’s luminosity. Here it also becomes apparent how quickly more massive stars ($M_{\text{final}} \geq 0.6 M_{\odot}$) evolve along the tracks compared to less massive stars, for example at $Z = 0.001$: two data points are separated by 50 yr, which means that after only a little more than 100 yr, a central star of mass $0.8 M_{\odot}$ reaches its peak temperature. As a result, even though more massive stars have the potential of developing brighter PNe, the likelihood of observing such a PN in its bright stage is much lower for more massive stars due to their fast evolution.

The PN model by Valenzuela et al. (2019) was originally developed for use with the post-AGB tracks from Miller Bertolami (2016) at a metallicity of $Z = 0.01$. As there is no obvious step in the model’s recipes where it would be trivial to add a direct dependence on metallicity, in this work we apply the PN model to central stars of all metallicities without modification. We leave it for future work to include the dependence of the nebular emission on the metallicity and oxygen abundance in the nebula (e.g., Dopita et al. 1992).

2.6. Number of planetary nebulae

The previous sections dealt with the modeling of a single PN based on the IMF, age and metallicity of the SSP. How many PN this SSP produces is additionally dependent on the total mass. For this the IMF is integrated between the initial mass obtained from the SSP age (Sect. 2.2) and the initial mass obtained from the SSP age minus 30 000 yr because those are the stars that are still in the PN phase. The integrated value is then multiplied with the total mass to obtain the expected total number of PNe in that SSP. The actual integer number is then determined by rounding down or up randomly based on the decimal places, for example an expected value of 10.2 would lead to 10 PNe being selected with an 80% chance and 11 PNe with a 20% chance.

The number of PNe is obtained after the initial stellar mass has been found from the lifetime function. The final mass and the PN properties are then determined individually for each of those PNe since values such as the post-AGB age or the absorbing factor can be different for PNe even within the same SSP.

3. The effect of metallicity and helium abundances

3.1. Metallicity

In the previous section it can be seen that multiple aspects of the emergence of PNe depend on the metallicity: For a given initial mass, more metal-rich stars remain on the MS and post-MS for a longer period of time (Fig. 1), and they lose more mass assuming the IFMR from Miller Bertolami (2016), leading to smaller final masses after the AGB phase (Fig. 2). For the post-AGB tracks at a given final mass, more metal-rich stars have lower luminosities and reach lower maximum temperatures before entering the cooling track (Fig. 3). Finally, while not depicted in this work, stars of a given final mass move along the Hertzsprung-Russell diagram at roughly the same speed, that is they heat up and cool down on a similar timescale (fig. 8 of Miller Bertolami 2016).

It is not directly clear from the individual relations themselves how the metallicity affects the central stars of the PNe when combining the lifetime function and the IFMR. To shed more light on this, we show how the final stellar mass depends on the age with varying metallicity in the left panel of Fig. 5. For a large age range, most of the metallicities lead to similar final masses: at ages of 2–7 Gyr all but $Z = 0.001$ lie closely

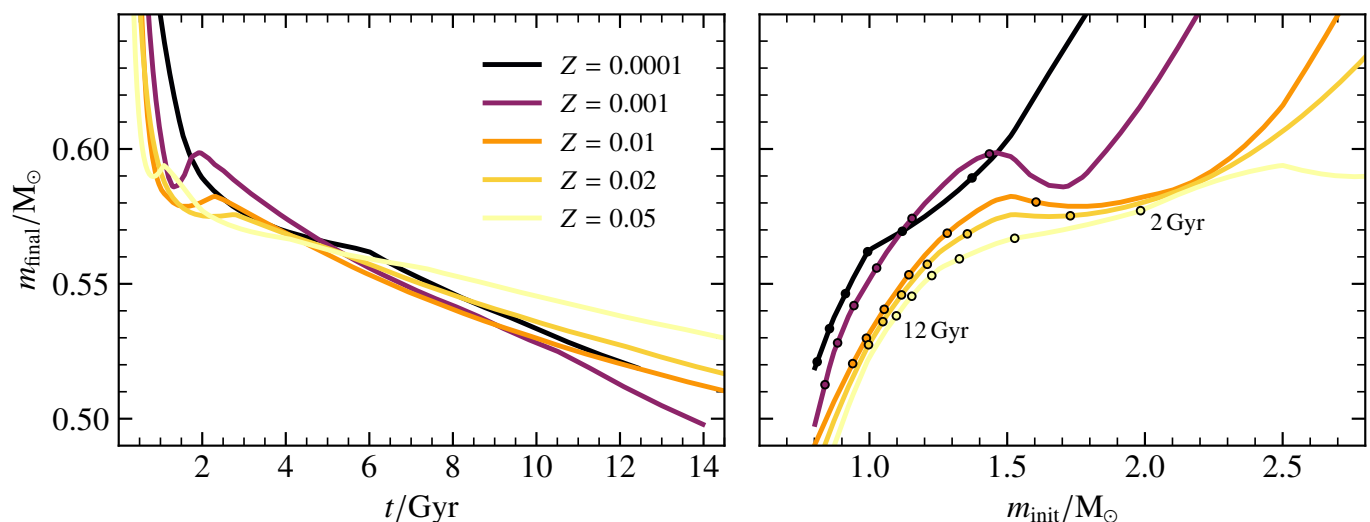


Fig. 5. Final masses as a function of stellar lifetime (left) and of initial mass (right) for selected metallicities ($Z = 0.0001, 0.001, 0.01, 0.02,$ and 0.05) based on the models of Miller Bertolami (2016). The final mass y-axis range is reduced to the primarily relevant values in the regime of older stellar populations of $t > 2$ Gyr. For the initial-to-final mass relation, the masses reaching the post-AGB phase after $t = 2, 4, 6, 8, 10,$ and 12 Gyr are marked with circles.

together, and at ages of 5–11 Gyr, all but $Z = 0.05$ lie closely together. Based on this model, this implies that there is a nearly universal final mass relation with age independent of metallicity for these ages, with variations of around $0.01\text{--}0.02 M_{\odot}$ at a given age. For lower and higher ages, however, the final masses begin to deviate more from one another. For stellar populations less than 2 Gyr old, stars becoming PNe that are more metal-rich tend to have smaller final masses. For ages above 8–10 Gyr and with $Z > 0.001$, the trend emerges under the current model assumptions that more metal-rich stellar populations produce PNe with larger final masses due to their longer lifetimes compared to their lower-mass counterparts. While these trends are not monotonic in the shown metallicity range, old stellar populations that are especially metal-rich above solar metallicity produce significantly more massive central stars of PNe than at lower metallicities, still reaching final masses of $0.55 M_{\odot}$ after 9 Gyr.

Based on these relations, we can now highlight the importance of taking the metallicity into account for especially metal-rich systems: if one were to follow the approach of some previous studies of assuming a fixed roughly solar-like metallicity of $Z = 0.01$ (e.g., Gesicki et al. 2018; Valenzuela et al. 2019), then for ages above 5 Gyr the final masses at that fixed metallicity would be systematically lower than if taking the correct higher metallicity into account (see the left panel of Fig. 5). The information can also be presented in the IFMR plot from Sect. 2.3 by marking specific times along the IFMRs at each metallicity. The right panel of Fig. 5 shows the IFMR for a more limited range of initial and final masses than shown in Fig. 2 where the points along the IFMRs are marked at equally spaced lifetimes between 2 and 12 Gyr. Especially at higher metallicities it can be seen that very old stellar populations with $t > 6$ Gyr have stars of higher initial and final masses reach the PN phase, resulting in old and metal-rich elliptical galaxies having more massive central stars of PNe than the old stellar population of a more metal-poor spiral galaxy, for example.

One caveat of the above conclusions based on the highest shown metallicity $Z = 0.05$ is that this metallicity lies outside the range originally modeled by Miller Bertolami (2016). Since those models only reached a metallicity of $Z = 0.02$, it cannot

simply be assumed that the extrapolation of the lifetime function to higher metallicities is applicable using the fit analytic relation (Sect. 2.2). One difficulty in this matter is that stellar evolution and in particular the AGB phase are still poorly understood for super-solar metallicity stars. This is largely due to such metal-rich stars being mostly observed only in the Galactic bulge or in M 31 for massive stars (e.g., Pietrinferni et al. 2013; McDonald et al. 2022). Some studies have run models for super-solar metallicity stars, including the PARSEC (Bressan et al. 2012) and BaSTI (Pietrinferni et al. 2013) stellar evolution models, additionally Althaus et al. (2009) investigated potential high-metallicity progenitors of WDs, and Nanni et al. (2014) ran super-solar metallicity models to study the dust production in pulsing AGB stars. As stated by Pietrinferni et al. (2013), there are differences between their BaSTI and the PARSEC models in part because of different initial helium abundance assumed in the models.

3.2. Helium abundance

Not only the initial helium abundance is uncertain: its scaling with the overall metallicity has been primarily measured at lower metallicities in the Milky Way and in H II regions. Mostly, studies have quantified a slope $\Delta Y/\Delta Z$ as the cosmic production rate of helium, which has been estimated to be between 1 and 3 (e.g., Jimenez et al. 2003; Izotov & Thuan 2004; Casagrande et al. 2007). However, not all authors assume a linear slope, especially at the lowest metallicities (e.g. Keszthelyi et al. 2024). While Miller Bertolami (2016) assumed a slope of 2 for the initial abundances of the stellar evolution models, it is unclear how exactly the helium-to-metallicity relation continues beyond the upper metallicity of $Z = 0.02$. Casagrande et al. (2007) even suggest that the slope becomes smaller towards higher metallicities, though the large uncertainties of the helium abundances and the metallicities make it difficult to draw definite conclusions on the true relation.

For these reasons, we ran two additional models following the procedure by Miller Bertolami (2016) with a super-solar metallicity of $Z = 0.05$. The first assumes the same linear relation between the helium abundance Y and metallicity Z of $Y = 0.245 + 2Z$ (i.e.,

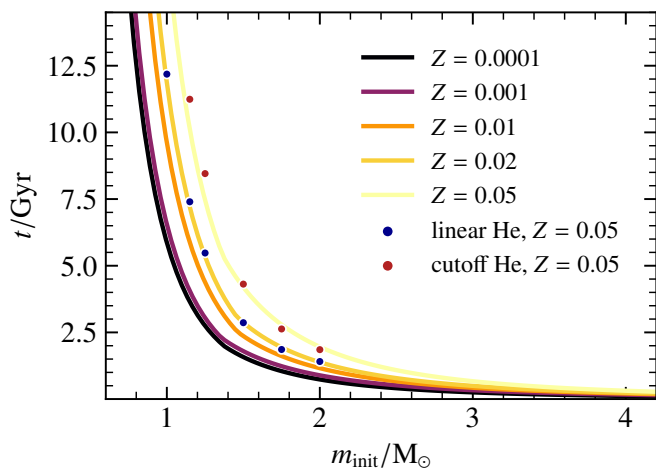


Fig. 6. Lifetime function of stars until they reach the post-AGB phase as a function of their initial mass. The lines are the fit relations to the models of Miller Bertolami (2016) with original metallicities of $Z = 0.0001, 0.001, 0.01,$ and $0.02,$ as in Fig. 1. Here the extrapolation of these fits to $Z = 0.05$ is also shown. The points are the results of newly run models following the procedure of Miller Bertolami (2016) for $Z = 0.05,$ and the lines are the fit relations to those data points. The linear helium abundance is at $Y = 0.345$ and the cutoff helium abundance at $Y = 0.285.$ The thick lines are at the same metallicities as the ones from the original models ($Z = 0.0001, 0.001, 0.01,$ and 0.02) and the thin lines are at $Z = 0.00001, 0.0003, 0.003,$ and $0.014,$ where the latter three values are the logarithmic midpoints of the original metallicities.

$Y = 0.345,$ linear He), whereas the second assumes that a saturation of helium is reached at the linearly determined value at $Z = 0.02$ (i.e., $Y = 0.285,$ cutoff He). The lifetime functions of the MS and post-MS for stars with these initial abundances as a function of the initial stellar mass are shown in Fig. 6 as the blue (linear He) and red (cutoff He) data points. Additionally, the values from the analytic relation obtained in Sect. 2.2 are shown as lines for the original four metallicities as well as for the extrapolated metallicity $Z = 0.05.$ We find that the blue linear helium data points at $Z = 0.05$ lie very close to the relation at the lower metallicity $Z = 0.02$ (light-orange line), whereas the red cutoff helium data points at $Z = 0.05$ also correspond to the extrapolated analytical function at $Z = 0.05$ (yellow line).

The newly run models show that the lifetime not only depends on metallicity, but is also heavily influenced by the helium abundance at $Z = 0.05.$ Another finding is that the overall trend of the lifetimes increasing with metallicity is not valid when extrapolating the linear relation between Y and Z beyond $Z = 0.02.$ This can be qualitatively explained by the following: in general, an increase of Z leads to higher bound-free opacities in the star, which lowers the radiative energy transport and overall luminosity. More metal-rich stars thus spend more time on the MS and post-MS. This is the case at lower metallicities, where the hydrogen abundance only minimally increases with higher $Z.$ However, at higher metallicities, a relative increase of Z results in a significantly larger change of the helium abundance following the linear relation of $Y = 0.245 + 2Z.$ As the hydrogen abundance is given by $X = 1 - Y - Z,$ the higher value of Y means that the total amount of available hydrogen is decreased, resulting in less fuel for the MS and thus shorter MS lifetimes. Moreover, a higher helium abundance implies a higher mean molecular weight of the stellar material. Due to the high sensitivity of luminosity on the molecular weight ($L \propto \mu^4;$ Kippenhahn et al. 2013), this leads to a larger luminosity and faster fuel consumption. In sum-

mary, when extrapolating the linear relation between Y and $Z,$ the stellar lifetime increases with metallicity until the rising helium abundance counteracts that effect, leading to similar lifetimes at $Z = 0.05$ and $Z = 0.02.$ In contrast, letting the helium abundance saturate and stay constant for values of $Z \geq 0.02$ means that the lifetimes continue to increase with metallicity.

For the saturated (cutoff) helium abundance, it is interesting that the simulated MS and post-MS lifetimes are overall very similar to the analytically computed values at $Z = 0.05$ for stars with initial masses $M_{\text{init}} \gtrsim 1.5 M_{\odot},$ but slightly higher at lower masses. This indicates that the extrapolation based on the lower metallicities (i.e., the analytic function that was fit to the original data points) corresponds to a slightly higher helium abundance than the saturated helium simulation. A thorough analysis of how the helium abundances affect the stellar lifetimes and the resulting PN populations is beyond the scope of this paper, however. It will be the subject of a future study.

Due to the poor observational constraints with respect to the Y - Z relation, we conclude that the analytically derived lifetime function from Sect. 2.2 at super-solar metallicities is still consistent with the stellar evolution simulations within the uncertainties of the observed helium abundances. Moreover, there is recent observational evidence for the helium abundance to saturate beyond a certain metallicity as measured for Omega Centauri (Clontz et al. 2024). First evidence supporting the usage of this function even at high metallicities is presented by Valenzuela et al. (2024), where the fiducial model of PICS was applied to several galaxies from a cosmological simulation, spanning a wide range of star formation histories, ages, and metallicities. The thereby obtained PN populations and their PNLF are consistent with observations and give a robust view of PNe, as will be fully shown in detail in the next paper of this series (Valenzuela et al. in prep.). In a future study we will further investigate how different assumptions regarding the helium abundances affect the PN populations of galaxies with different star formation histories in detail. Comparing the observed PN populations with modeled PNe based on simulated galaxies may even provide an independent way of probing the production rate of helium at high metallicities. In the following sections we apply the analytic function from Sect. 2.2 for all metallicities.

4. Single stellar population PNLFs

In Sect. 3 we have highlighted the importance of the metallicity and helium abundance when considering some of the individual blocks required to model the PNe within a stellar population. We now showcase how the SSP age and metallicity affect the resulting PNe by exploring the parameter space for the fiducial PICS model. For this, we paired ten SSP ages between $t_{\text{age}} = 0.25$ and 13 Gyr with six metallicities between $Z = 0.0001$ and 0.08 to run PICS on and obtain corresponding PNLFs. To overcome the stochastic nature of the PN model itself with respect to the post-AGB age and the absorbing factor that determines the opacity of the nebula, we ran PICS on 10^6 stars for each pair of age and metallicity, with equally spaced post-AGB ages between 0 and 30 000 yr. Figure 7 shows the PNLFs for a grid of SSPs with different ages (constant age per row) and metallicities (constant metallicity per column), that is the $M(5007)$ histograms for the 10^6 PNe, as the black lines. The black lines therefore represent the PNLFs for a fixed number (10^6) of PNe with the same age and metallicity.

Since the PN central stars have different initial and final masses depending on the age and metallicity (the final masses are noted in the bottom left corner of each panel in Fig. 7), varying

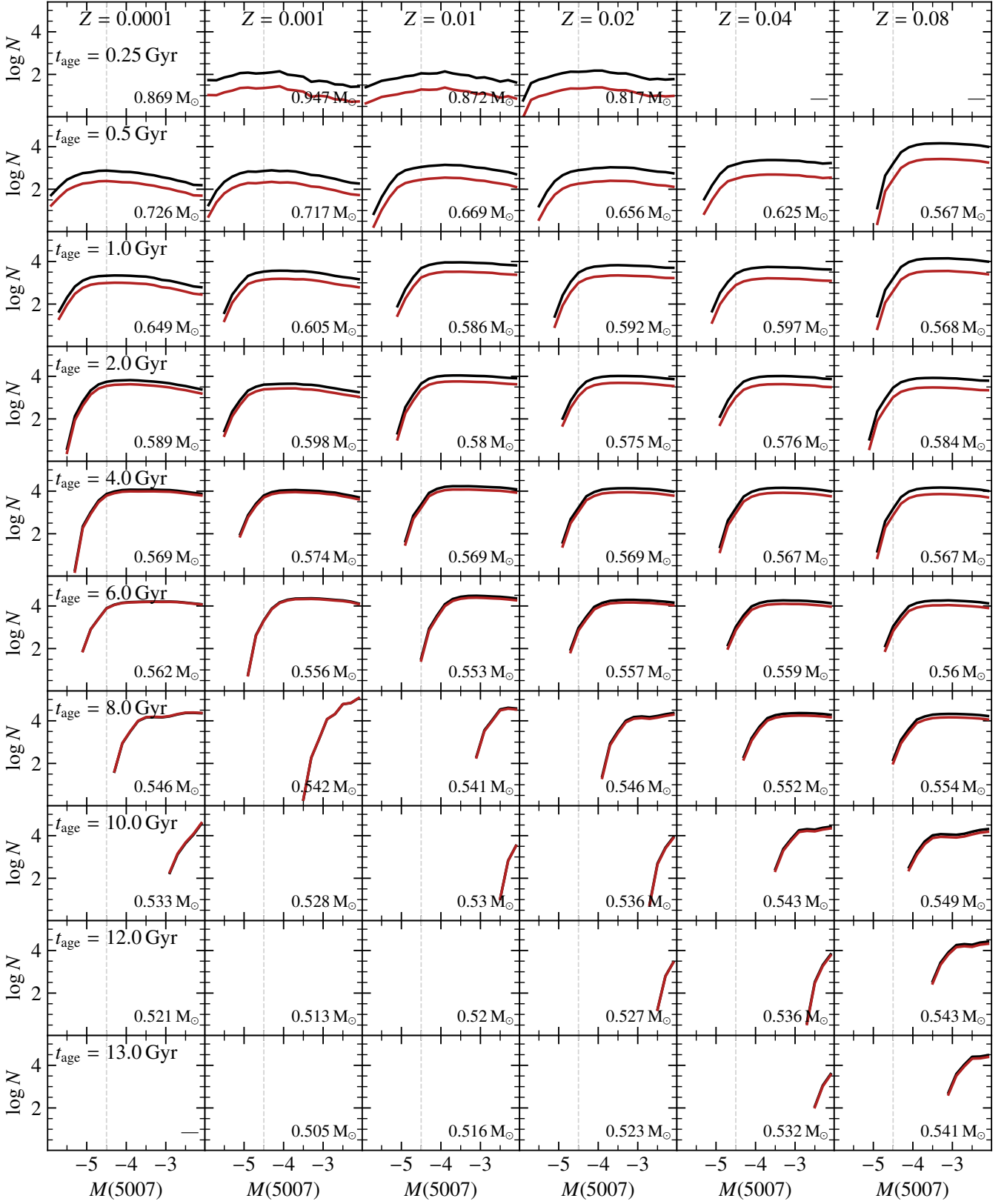


Fig. 7. Single stellar population PNLFs depending on the age and metallicity for the fiducial model. Rows correspond to the different ages and columns to the metallicities and are indicated by the text labels in the respective first row and column panels. The final masses resulting from the initial masses are computed from the IFMR of Miller Bertolami (2016) and are stated in the lower left corner of each panel. In the cases where the initial mass values lie outside the modeled range, only a dash is shown (this is only the case for two panels in the top right and one in the bottom left). The black lines are the PNLFs obtained from 10^6 stars of the respective final mass with equally spaced post-AGB ages between 0 and 30 000 yr. The red PNLFs are rescaled for a Chabrier IMF (Chabrier 2003), such that they can be compared relative to each other (i.e., the more massive stars are less frequent than lower-mass stars). The bright-end cutoff is marked by the vertical gray dashed line at $M(5007) = -4.5$.

numbers of PNe are expected to be found if the total SSP mass is kept constant, based on the IMF: more massive stars are less frequent than less massive stars. As a result, there would for example be fewer than 10^6 PNe with an initial mass of $M_{\text{init}} = 2.0 M_{\odot}$ compared to an initial mass of $M_{\text{init}} = 1.2 M_{\odot}$. To visualize the expected PNLFs at constant total SSP mass, we show these as red lines in Fig. 7, where the red PNLFs are lowered compared to the black PNLFs at fixed PN number when the initial mass is larger, based on the Chabrier (2003) IMF. The normalization is set such that the red PNLFs (fixed total SSP mass) made up of stars with an initial mass of roughly $1 M_{\odot}$ lie on the black PNLFs (fixed PN number). Since any given stellar population is made up of many SSPs, any observed or simulated PNLF is in fact a superposition of these SSP PNLFs.

The first finding is that not all combinations of age and metallicity contribute to the bright end of the PNLF at around $M(5007) = -4.5$ (e.g., Ciardullo 2012), marked by the vertical gray dashed lines. Especially old stellar populations with ages of $t_{\text{age}} \geq 8\text{--}10$ Gyr generally produce fainter PNe, though especially low ($Z = 0.0001$) and high ($Z > 0.04$) metallicities can lead to a larger population of bright PNe with $M(5007) < -2$ compared to intermediate metallicities at those ages. The final masses of the PNe in these stellar populations for the most part lie around $M_{\text{final}} \sim 0.51\text{--}0.55 M_{\odot}$, which lies well below the expected maximum final masses of older observed stellar population from previous studies needed to explain the brightest PNe (e.g., Méndez 2017; Valenzuela et al. 2019).

For intermediate age stellar populations with $t_{\text{age}} \sim 2\text{--}8$ Gyr, the bright end of the PNLF is well populated with PNe, with brighter nebulae being reached for lower ages. A similar trend as for the older aged populations can also be seen here (i.e., fewer bright PNe at intermediate metallicities), though not as significant. Interestingly, there is a maximum of the PNLF between $M(5007) = -4.5$ and -4.0 for a number of the age-metallicity combinations in this intermediate-age regime, with a slow decline of the PNLF towards fainter PNe. All of the SSP PNLFs here feature the recognizable typical shape of observed PNLFs, just with shifts towards brighter or fainter magnitudes. Here the final masses lie between around 0.55 and $0.59 M_{\odot}$, approximately in the expected maximum central star final mass range for old stellar populations based on modeling PNe in mock stellar populations (Valenzuela et al. 2019).

The younger stellar populations at $t_{\text{age}} \lesssim 1$ Gyr only feature the typical PNLF shape at the higher metallicities, whereas lower-metallicities lead to much brighter PNe existing even well beyond $M(5007) = -5.0$. The absolute numbers are overall much lower than for older stellar populations, which is a result of the much faster evolution along the post-AGB tracks for these more massive central stars ($M_{\text{final}} \gtrsim 0.6$). The stars reside on the heating track for only a short period of time (see the widely spaced data points in Fig. 4 for the more massive central stars) before cooling down and dropping in luminosity, thus making bright nebulae around those massive stars rather rare. For these younger ages, the normalization according to an IMF further reduces the relative number of PNe compared to the panels for the older stellar populations, as seen by the red line (fixed total SSP mass) increasingly separating from the black line (fixed PN number).

The fact that the PNLFs can also reach much brighter magnitudes is very likely due to the PN model of Valenzuela et al. (2019) not incorporating internal dust extinction. The internal dust extinction has been observed to rise with increasing PN brightness, thus pushing the brightest PNe back down to the bright end cutoff (e.g., Davis et al. 2018; Jacoby & Ciardullo in prep.).

For some nearby galaxies it has been possible to measure a statistically complete PNLF down to six magnitudes below the bright cutoff (e.g., Reid & Parker 2010; Bhattacharya et al. 2019), which has revealed significant variations of the PNLF shape at its faint end. We show the same grid of PNLFs up to a magnitude of $M(5007) = +2$ in Appendix B, which is around 6.5 magnitudes below the bright end of the PNLF. These will be relevant in upcoming studies to compare the models with such nearby deep observations and provide a means for interpreting the variations of the PNLF shape. We highlight two insights from the extended magnitude PNLF grid: first, we find the dip or “camel” shape previously found in some galaxies with recent star formation like the Magellanic Clouds or NGC 300 (Jacoby & De Marco 2002; Reid & Parker 2010; Peña et al. 2012; Soemmitro et al. 2023) and simulations of mock stellar populations with more massive central stars (Méndez et al. 2008; Valenzuela et al. 2019). Here we find that this dip already arises from the PNLF of a sole SSP and is not just the result of multiple stellar populations overlapping with each other, as has for example been proposed by Rodríguez-González et al. (2015). The physical reason for the dip is that more massive post-AGB stars can host brighter PNe on their heating track than lower-mass stars, but their extremely fast evolution leads to them cooling down very quickly, resulting in a rapid decline of the [O III] emission before reaching a moderate brightness, where their evolution slows down and PNe accumulate, which is where the PNLF rises again. Second, the differences in shape and slope found at the faint end of the PNLF in observations indicate that these individual SSP PNLFs will help better understand and interpret the different behaviors found at the faint end of the PNLF, for example for PN populations in M31 and its outskirts (Bhattacharya et al. 2021).

In Sect. 2.3 we presented several IFMRs in addition to the one by Miller Bertolami (2016) used in the fiducial PICS model, namely those by Cummings et al. (2018), Cunningham et al. (2024), and Hollands et al. (2024). In Fig. 8 we show the consequence of adopting an IFMR that does not depend on metallicity by using the latter three IFMRs instead of that of the fiducial PICS model by Miller Bertolami (2016). The black lines are the same as those in Fig. 7 from the fiducial PICS model, while the colored lines correspond to the obtained PNLFs using the IFMRs of Cummings et al. (2018), Cunningham et al. (2024), and Hollands et al. (2024). The different IFMRs only show a similar PNLF for younger ages of around $t_{\text{age}} \lesssim 6$ Gyr, and only the PICS fiducial IFMR shows a deviating behavior at higher metallicities in this age range with a larger number of PNe, but at the same time a fainter bright end of the PNLF. The values of age and metallicity where agreement is found between the PNLFs roughly correspond to the initial mass range of $m_{\text{init}} \gtrsim 1.3 M_{\odot}$ in which the alternative IFMRs do not lead to higher final masses than at even the lowest metallicities of the fiducial models (Fig. 2). In contrast, for lower initial masses and thus for older stellar populations, Fig. 2 shows that in particular the IFMR by Cummings et al. (2018) surpasses the final mass values of the fiducial model at all metallicities. At the lowest initial masses around $m_{\text{init}} \approx 0.9 M_{\odot}$, both the models of Cummings et al. (2018) and Cunningham et al. (2024) show higher final masses than the fiducial models because their values result from linear fits in this mass range without a drop towards lower initial masses (in contrast to the fiducial model and that by Hollands et al. 2024). Since this leads to final masses of $m_{\text{final}} \gtrsim 0.55 M_{\odot}$, even such old low-mass stars are able to produce bright PNe, as seen by the bright PNe in turquoise and red in Fig. 8 for older systems of $t_{\text{age}} \gtrsim 8$ Gyr. Overall, the PNe produced with the IFMR by Cummings et al. (2018) can be the brightest at a given age and metallicity. The PNLFs

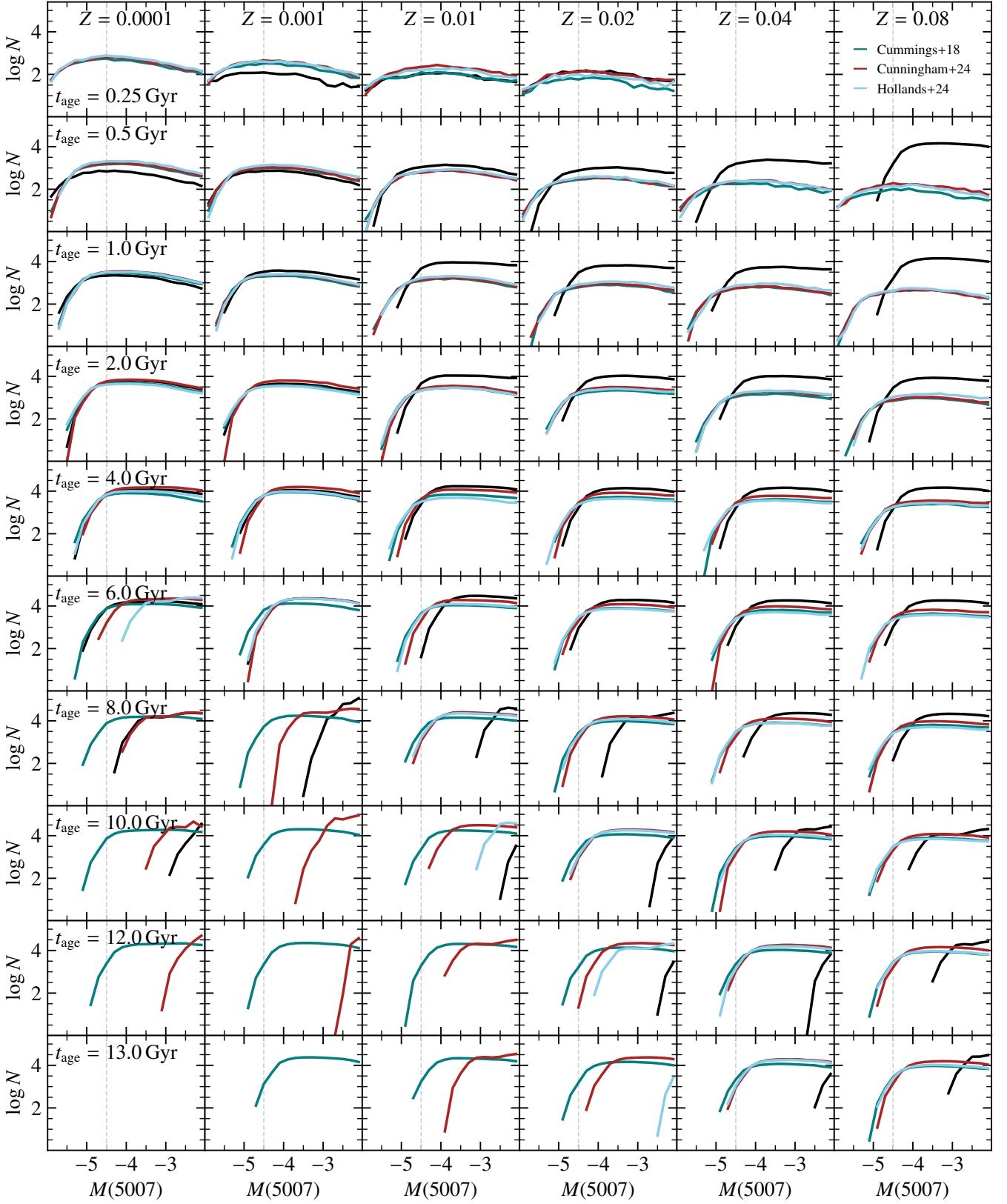


Fig. 8. Single stellar population PNLFs depending on the age and metallicity for the fiducial model (black) and with variations of the IFMR (colored). The IFMRs are from [Miller Bertolami \(2016\)](#) in black, and [Cummings et al. \(2018\)](#), [Cunningham et al. \(2024\)](#), and [Hollands et al. \(2024\)](#) in turquoise, red, and light blue, respectively. Rows correspond to the different ages and columns to the metallicities and are indicated by the text labels in the respective first row and column panels. The lines are the PNLFs obtained from 10^6 stars of the respective final mass with equally spaced post-AGB ages between 0 and 30 000 yr. The bright-end cutoff is marked by the vertical gray dashed line at $M(5007) = -4.5$.

obtained with their IFMR are surprisingly similar in bright end and shape across most ages and metallicities with only minor shifts of the bright end. Differences in the bright end cutoff of up to half a magnitude can be found between the different IFMRs for $t_{\text{age}} = 6$ Gyr, one magnitude at 8 Gyr, and more than 2–3 magnitudes in stellar populations older than 10 Gyr.

Despite the sharp drop in the IFMR of [Hollands et al. \(2024\)](#) towards lower masses in the range of $m_{\text{init}} \lesssim 1 M_{\odot}$, which is even more extreme than the fiducial model shows, the light blue lines for [Hollands et al. \(2024\)](#) at high ages and metallicities show that bright PNe can still be produced (bottom right panels in Fig. 8). This is a consequence of the metallicities influence on the lifetime function, which is that higher metallicities lead to more massive stars reaching the post-AGB phase for a given SSP age. Because of the drastic drop of the final mass with lower initial masses, old low-metallicity SSPs do not produce bright PNe when using the IFMR by [Hollands et al. \(2024\)](#), leading to a lack of the light blue PNLFs in the bottom left panels in Fig. 8.

For the younger ages at high metallicities (top right panels), it may seem curious that all alternative IFMRs lead to similar bright PNLFs, whereas the fiducial IFMR by [Miller Bertolami \(2016\)](#) leads to a slightly dimmer bright end, but a significantly higher number of PNe. The reason for this can be understood by considering Fig. 2. For young ages, the initial masses are above $2 M_{\odot}$. In this range, the high metallicity fiducial IFMRs show much lower final masses than the alternative IFMRs. The final masses are still high enough to produce relatively bright PNe, but not quite as bright as those obtained with higher final masses. However, the stars with lower final masses move more slowly across the Hertzsprung-Russell diagram before cooling down, thus allowing the nebula to survive for a longer period of time. The result is a larger number of PNe that can be observed.

The grid of PNLFs with different assumed IFMRs shows that the assumed IFMR strongly affects the PNLF that can be expected from a given stellar population, in particular for older systems. It is interesting that it is the regime of old stellar populations, where the abundance of PNe at the bright end has been a puzzle for a long time, that shows the highest sensitivity to the IFMR. This shows that the IFMR will play a significant role in the understanding of PNe in old stellar populations. Finally, even though the metallicity is not considered for the alternative IFMRs themselves, the metallicity dependence of the lifetime function and the post-AGB tracks leads to a shift of the bright end of the PNLFs, which can mostly be summarized as having a brighter PNLF cutoff at higher metallicities.

5. Summary and Conclusion

This first paper in a series introduces PICS (PNe In Cosmological Simulations), a modular framework that models the PN population contained within an SSP. The SSP is described by its total mass, age, IMF, and optionally by its metallicity and/or further abundances. For our fiducial model, we consider the SSP metallicity mass ratio and use the metallicity-dependent lifetime function, IFMR, and post-AGB tracks from [Miller Bertolami \(2016\)](#) to model the central stars of the PNe. The nebula and its [O III] emission are modeled using the method from [Valenzuela et al. \(2019\)](#). PICS thus produces the main observable quantity of extragalactic PNe and can be employed to compare theoretical models and hydrodynamical cosmological simulations with observations, which in turn can be used to interpret the properties of the PNe and underlying stellar populations.

We show how the initial metallicity of the star affects the stellar evolution relevant to PNe: higher metallicities lead to more

massive stars reaching the post-AGB phase later than their lower-metallicity counterparts, while the final masses after the AGB phase are lower at constant initial mass. Higher metallicities also lead to lower luminosities and temperatures of the central stars for a fixed final mass. Considering both the lifetime function and the IFMR, the effect of the metallicity is strongest at ages below 4 Gyr, where lower metallicities lead to more massive PN central stars, and at higher ages above 6 Gyr, where higher metallicities lead to more massive central stars. The effect on final mass becomes strongest at very young and at very old ages. The final mass is important for the maximal brightness of $M(5007)$ that can be reached throughout the post-AGB phase and reaching higher final masses will increase the probability of finding such a PN at the bright end of the PNLF. Furthermore, these relations provide the first indications that the metallicity is relevant for older stellar populations, in particular as these are oftentimes more metal-rich in massive elliptical galaxies than in disk galaxies like our own Milky Way.

One important finding of this work is that for high-metallicity stars, the metallicity is not the only property affecting the lifetime of stars. While higher metallicities generally do increase the opacity of the star, leading to longer lifetimes, the accompanying increase of the helium abundance counteracts this trend due to higher luminosities and less available fuel. As the relation of helium abundance with metallicity is still poorly constrained from observations, in particular at high metallicities, we explored the parameter space ranging from a linearly increasing helium abundance with metallicity to a constant helium abundance of $Y = 0.285$ above a metallicity of $Z = 0.02$. Such a constant helium abundance above a certain metallicity would be in line with recent observations of the metallicity of the stellar population of the globular cluster Omega Centauri ([Clontz et al. 2024](#)).

Assuming the linear relation, the lifetime function does not lead to longer timescales at higher metallicities above $Z = 0.02$ anymore, whereas assuming a saturation of the helium abundance results in longer lifetimes at $Z > 0.02$. The helium abundance relation is therefore especially relevant for metal-rich stellar populations, as it governs how the lifetime function behaves for the individual stars. A higher helium abundance causes shorter lifetimes, leading to less massive stars becoming PNe after a given time at fixed metallicity. This in turn means that the brightest possible magnitudes $M(5007)$ are dimmer. If the helium abundance is capped, however, the stellar lifetimes increase, leading to more massive central stars at older ages for super-solar metallicity stellar populations. Based on the metallicities originally used by [Miller Bertolami \(2016\)](#) of $Z = 0.0001$ – 0.02 , we derived an analytic expression for the lifetime function, whose extrapolation lies between the simulated values for linear and constant helium abundance relations, but closer to the latter. Thus, for the fiducial model, we pick the constant helium abundance relation due to it lying closer to the analytic function. Since longer lifetimes of metal-rich stars increase the occurrence of bright-end PNe in old stellar populations, our findings indicate that a saturation of the helium abundance at high metallicities could be part of the solution for the universal bright-end cutoff of the PNLF. Indeed, this scenario would be in line with the recent observations by [Clontz et al. \(2024\)](#). The implications would be that high-metallicity stars have longer lifetimes than expected from models assuming non-saturated helium abundances. In future studies we will extend our stellar grids to include the effect of the helium abundance consistently with the prediction from cosmological models.

To obtain a complete overview of how the SSP metallicity and age affect the resulting PN population, we produced a grid of PNLFs, each corresponding to a fixed pair of metallicity and age.

The PNLF shapes are generally consistent with each other and have a varying bright end cutoff: older SSPs generally contain less luminous PNe. However, at older ages above 6 Gyr, higher metallicities again lead to brighter PNe forming. In addition, at almost all ages the lowest metallicities of $Z = 0.0001$ and $Z = 0.001$ also lead to somewhat brighter PNe. In particular, the brighter old and metal-rich PNe could in part explain how old elliptical galaxies still retain a similar bright end of the PNLF compared to disk galaxies as they tend to be especially metal-rich. The grids of SSP PNLFs presented in this work set the theoretical foundation for interpreting the relations of the observed PNLF bright end with properties of the underlying stellar populations with respect to their age and metallicity.

We also present a grid of extended PNLFs down to six magnitudes below the bright end cutoff, which are needed for comparison and interpretation of PN studies of Local Universe galaxies, where it has been possible to obtain statistically complete samples even of very faint PNe, for example in the LMC or M31 (Reid & Parker 2010; Bhattacharya et al. 2021). The extended PNLFs reveal that the “dip” or “camel shape” of the PNLF with a minimum at around $M(5007) \approx -2-0$, which has previously been seen in observations (e.g., Jacoby & De Marco 2002; Reid & Parker 2010; Peña et al. 2012; Soemito et al. 2023) and models (e.g., Méndez et al. 2008; Valenzuela et al. 2019) is in fact an intrinsic property of PNe with more massive central stars and arises even in SSPs. It is thereby not only a result of two or more modes of PNLFs from multiple stellar populations, as has been suggested by Rodríguez-González et al. (2015). Of course, any real PNLF is a superposition of SSP PNLFs, which can lead to an even larger variety of observed faint PNLF shapes. This carries the potential of being another independent diagnostic tool for investigating the underlying star formation history and metallicity properties of galaxies and their formation histories.

Finally, we studied how different IFMRs affect the resulting PN populations by considering metallicity-independent IFMRs determined from the solar neighborhood in the Milky Way in addition to the relation used for the fiducial model from Miller Bertolami (2016). The various IFMRs do not change the SSP PNLFs much for younger stellar populations of $\lesssim 6$ Gyr. However, at larger ages the constant IFMRs mostly lead to brighter PNe being produced, in part even reaching the bright end cutoff for the IFMR by Cummings et al. (2018). The reason for this is that some of these IFMRs do not see the final stellar masses drop as steeply towards low initial masses as the relations by Miller Bertolami (2016). Furthermore, the lack of metallicity dependence means that at high metallicities the PN central stars are more massive than when employing the metallicity-dependent IFMR, in turn leading to on average brighter PNe. The implications for the existence of bright PNe in old stellar populations are very important: The IFMR, in particular at initial masses of $M_{\text{init}} \lesssim 1.2 M_{\odot}$, plays a significant role in how massive the central stars are and therefore how bright the PNe can get. Getting better constraints and developing a more robust theoretical understanding of the mass loss in the AGB phase is therefore essential for explaining the observed bright end of the PNLF in old stellar populations.

With PICS, we have laid the groundwork for populating cosmological simulations with PNe, thereby producing PN populations based on self-consistent star formation histories within a cosmological context. On the theoretical side, this allows us to make predictions for the PNLF behavior based on statistically significant samples of galaxies with diverse morphologies and star formation histories, which will aid our understanding of the universal bright end of the PNLF. Furthermore, the modular

structure of PICS makes parameter studies possible, where controlled changes to one specific block in the pipeline can be used to understand its effect on the resulting PN population, just as done for the IFMR in this work. For the observational side, it will be possible to compare the modeled PN populations to observations by identifying appropriate simulated galaxy analogues, and to offer an interpretation for the observed PNe and their properties.

To conclude, we have shown in this study that it is essential to account for both the metallicity and helium abundances in PNe models, as well as improving the observations and models of the IFMR. These factors all particularly affect the brightest PNe, leading us one step further in our understanding of the universal bright end of the PNLF, which we will explore in more detail in future studies.

Acknowledgements. We thank Souradeep Bhattacharya, George Jacoby, Taziu Hoffmann, Rolf-Peter Kudritzki, and Joachim Puls for helpful comments and discussions, and Tim Cunningham for providing us with his data tables of the IFMR. LMV acknowledges support by the German Academic Scholarship Foundation (Studienstiftung des deutschen Volkes) and the Marianne-Plehn-Program of the Elite Network of Bavaria. M3B is partially funded by CONICET and Agencia I+D+i through grants PIP-2971 and PICT 2020-03316, and by CONICET-DAAD 2022 bilateral cooperation grant number 80726. This research was supported by the Excellence Cluster ORIGINS, funded by the Deutsche Forschungsgemeinschaft under Germany’s Excellence Strategy – EXC-2094-390783311. The following software was used for this work: Julia (Bezanson et al. 2017), DataInterpolations.jl (Bhagavan et al. 2024), Interpolations.jl (Holy et al. 2022), matplotlib (Hunter 2007), and numpy (Harris et al. 2020).

References

- Althaus, L. G., Panei, J. A., Romero, A. D., et al. 2009, *A&A*, 502, 207
 Asplund, M., Grevesse, N., Sauval, A. J., & Scott, P. 2009, *ARA&A*, 47, 481
 Bezanson, J., Edelman, A., Karpinski, S., & Shah, V. B. 2017, *SIAM Review*, 59, 65
 Bhagavan, S., de Koning, B., Maddhashiya, S., & Rackauckas, C. 2024, *Journal of Open Source Software*, 9, 6917
 Bhattacharya, S., Arnaboldi, M., Gerhard, O., et al. 2021, *A&A*, 647, A130
 Bhattacharya, S., Arnaboldi, M., Hartke, J., et al. 2019, *A&A*, 624, A132
 Bloeker, T. 1995, *A&A*, 299, 755
 Bressan, A., Marigo, P., Girardi, Léo., et al. 2012, *MNRAS*, 427, 127
 Caffau, E., Ludwig, H. G., Steffen, M., Freytag, B., & Bonifacio, P. 2011, *Sol. Phys.*, 268, 255
 Casagrande, L., Flynn, C., Portinari, L., Girardi, L., & Jimenez, R. 2007, *MNRAS*, 382, 1516
 Chabrier, G. 2003, *PASP*, 115, 763
 Ciardullo, R. 2010, *PASA*, 27, 149
 Ciardullo, R. 2012, *Ap&SS*, 341, 151
 Ciardullo, R., Feldmeier, J. J., Jacoby, G. H., et al. 2002, *ApJ*, 577, 31
 Ciardullo, R. & Jacoby, G. H. 1992, *ApJ*, 388, 268
 Ciardullo, R., Jacoby, G. H., Ford, H. C., & Neill, J. D. 1989, *ApJ*, 339, 53
 Ciardullo, R., Sigurdsson, S., Feldmeier, J. J., & Jacoby, G. H. 2005, *ApJ*, 629, 499
 Clontz, C., Seth, A. C., Wang, Z., et al. 2024, arXiv e-prints, arXiv:2412.09783
 Cummings, J. D., Kalirai, J. S., Tremblay, P. E., Ramirez-Ruiz, E., & Choi, J. 2018, *ApJ*, 866, 21
 Cunningham, T., Tremblay, P.-E., & W. O’Brien, M. 2024, *MNRAS*, 527, 3602
 Davis, B. D., Ciardullo, R., Jacoby, G. H., Feldmeier, John. J., & Indahl, B. L. 2018, *ApJ*, 863, 189
 Dopita, M. A., Jacoby, G. H., & Vassiliadis, E. 1992, *ApJ*, 389, 27
 Douglas, N. G., Arnaboldi, M., Freeman, K. C., et al. 2002, *PASP*, 114, 1234
 Gesicki, K., Zijlstra, A. A., & Miller Bertolami, M. M. 2018, *Nature*, 2, 580
 Harris, C. R., Millman, K. J., van der Walt, S. J., et al. 2020, *Nature*, 585, 357
 Hartke, J., Arnaboldi, M., Longobardi, A., et al. 2017, *A&A*, 603, A104
 Hollands, M. A., Littlefair, S. P., & Parsons, S. G. 2024, *MNRAS*, 527, 9061
 Holy, T., Kittisopikul, M., Wadell, A., et al. 2022, *Zenodo*
 Hunter, J. D. 2007, *Computing in Science and Engineering*, 9, 90
 Izotov, Y. I. & Thuan, T. X. 2004, *ApJ*, 602, 200
 Jacoby, G. H. 1989, *ApJ*, 339, 39
 Jacoby, G. H., Ciardullo, R., & Ford, H. C. 1990, *ApJ*, 356, 332
 Jacoby, G. H., Ciardullo, R., Roth, M. M., Arnaboldi, M., & Weilbacher, P. M. 2024, *ApJS*, 271, 40
 Jacoby, G. H. & De Marco, O. 2002, *AJ*, 123, 269
 Jimenez, R., Flynn, C., MacDonald, J., & Gibson, B. K. 2003, *Science*, 299, 1552

- Keszthelyi, Z., Puls, J., Chiaki, G., et al. 2024, MNRAS, 533, 3457
- Kippenhahn, R., Weigert, A., & Weiss, A. 2013, *Stellar Structure and Evolution*, 2nd edn., Astronomy and Astrophysics Library (Heidelberg: Springer Berlin)
- Kreckel, K., Groves, B., Bigiel, F., et al. 2017, ApJ, 834, 174
- Li, H., Mao, S., Cappellari, M., et al. 2018, MNRAS, 476, 1765
- Longobardi, A., Arnaboldi, M., Gerhard, O., et al. 2013, A&A, 558, A42
- Marigo, P., Cummings, J. D., Curtis, J. L., et al. 2020, Nature, 4, 1102
- Marigo, P., Girardi, L., Weiss, A., Groenewegen, M. A. T., & Chiosi, C. 2004, A&A, 423, 995
- McDonald, S. L. E., Davies, B., & Beasor, E. R. 2022, MNRAS, 510, 3132
- Méndez, R. H. 2017, in IAU Symposium, Vol. 323, Planetary Nebulae: Multi-Wavelength Probes of Stellar and Galactic Evolution, eprint: arXiv:1610.08625, 298–302
- Méndez, R. H., Kudritzki, R. P., Ciardullo, R., & Jacoby, G. H. 1993, A&A, 275, 534
- Méndez, R. H. & Soffner, T. 1997, A&A, 321, 898
- Méndez, R. H., Teodorescu, A. M., Schönberner, D., Jacob, R., & Steffen, M. 2008, ApJ, 681, 325
- Miller Bertolami, M. M. 2016, A&A, 588, A25
- Nanni, A., Bressan, A., Marigo, P., & Girardi, L. 2014, MNRAS, 438, 2328
- Padovani, P. & Matteucci, F. 1993, ApJ, 416, 26
- Peña, M., Reyes-Pérez, J., Hernández-Martínez, L., & Pérez-Guillén, M. 2012, A&A, 547, A78
- Pietrinferni, A., Cassisi, S., Salaris, M., & Hidalgo, S. 2013, A&A, 558, A46
- Pulsoni, C., Gerhard, O., Arnaboldi, M., et al. 2018, A&A, 618, A94
- Reid, W. A. & Parker, Q. A. 2010, MNRAS, 405, 1349
- Rekola, R., Richer, M. G., McCall, M. L., et al. 2005, MNRAS, 361, 330
- Renzini, A. 1981, Annales de Physique, 6, 87
- Renzini, A. & Buzzoni, A. 1986, in *Astrophysics and Space Science Library*, Vol. 122, Proceedings of the Fourth Workshop (Erice, Italy: Dordrecht, D. Reidel Publishing Co.), 195–231
- Rodríguez-González, A., Hernández-Martínez, L., Esquivel, A., et al. 2015, A&A, 575, A1
- Roth, M. M., Jacoby, G. H., Ciardullo, R., et al. 2021, ApJ, 916, 21
- Scheuermann, F., Kreckel, K., Anand, G. S., et al. 2022, MNRAS, 511, 6087
- Schönberner, D. 1983, ApJ, 272, 708
- Schönberner, D., Jacob, R., Steffen, M., & Sandin, C. 2007, A&A, 473, 467
- Soemito, A. A., Roth, M. M., Weilbacher, P. M., et al. 2023, A&A, 671, A142
- Soker, N. 2006, ApJ, 640, 966
- Souropanis, D., Chiotellis, A., Boumis, P., Jones, D., & Akras, S. 2023, MNRAS, 521, 1808
- Spriggs, T. W., Sarzi, M., Napiwotzki, R., et al. 2020, A&A, 637, A62
- Valenzuela, L. M., Méndez, R. H., & Miller Bertolami, M. M. 2019, ApJ, 887, 65
- Valenzuela, L. M., Remus, R.-S., Miller Bertolami, M. M., & Méndez, R. H. 2024, in IAU Symposium, Vol. 384, Planetary Nebulae: a Universal Toolbox in the Era of Precision Astrophysics, 1–1
- Vassiliadis, E. & Wood, P. R. 1994, ApJS, 92, 125
- von Steiger, R. & Zurbuchen, T. H. 2016, ApJ, 816, 13
- Yao, P. Z. & Quataert, E. 2023, ApJ, 957, 30

Appendix A: Post-AGB track interpolation

Here we present how the post-AGB tracks provided by [Miller Bertolami \(2016\)](#) are interpolated (see Sect. 2.4 for the corresponding section in the main text). For the post-AGB tracks, we take the output tables from [Miller Bertolami \(2016\)](#), which each consist of 101 points of equivalent position along the tracks in the Hertzsprung-Russel diagram, with precomputed luminosity, effective temperature, and post-AGB time since a temperature of $\log T_{\text{eff}}/\text{K} = 3.85$ was reached. The tables are available for between 12 and 20 final masses for each of the four metallicities $Z = 0.0001$ (12 between $M_{\text{final}} = 0.525$ and $0.800 M_{\odot}$), $Z = 0.001$, $Z = 0.01$, and $Z = 0.02$ (each of them have 20 tables for final masses between $M_{\text{final}} = 0.525$ and $1.000 M_{\odot}$). As we follow the approach of [Valenzuela et al. \(2019\)](#) in this work to define the post-AGB age as the time since a temperature of $T_{\text{eff}} = 25\,000$ K was reached, the precomputed post-AGB ages are shifted accordingly in the individual tables. To interpolate the tracks for arbitrary metallicities, final masses, and post-AGB ages, we perform linear interpolations on the logarithmic metallicity and the final mass to find the eight relevant equivalent points on the tracks corresponding to the two adjacent metallicities, final masses, and post-AGB ages. The luminosity and effective temperatures are then determined from these eight points by trilinear interpolation, the result of which can be seen in Fig. 3.

Appendix B: Extended PNLFs

In Fig. B.1 we show the same set of SSP PNLFs as in Fig. 7 for a grid of different ages and metallicities, just increasing the plotted magnitude range to fainter PNe at $M(5007) = +2$. Here it is much more obvious that most of the individual PNLFs drop towards fainter PNe and many in the young to intermediate age range ($t_{\text{age}} \lesssim 6$ Gyr) then again have a rising number of PNe towards the faintest magnitudes. This “camel” shape has previously been found in both observations and simulations of PNe, in particular in younger systems (e.g., [Jacoby & De Marco 2002](#); [Reid & Parker 2010](#); [Valenzuela et al. 2019](#)), though the dip in the SMC occurs at a slightly dimmer magnitude of $M(5007) \approx -0.5$ ([Jacoby & De Marco 2002](#)). This is consistent with the grid of PNLFs shown here, where the SSP models in Fig. B.1 show that this shape can also arise within a pure SSP and it is not dependent on the correct superposition of different SSP PNLFs. In contrast, it is possible to wash out the camel shape by combining multiple SSP PNLFs as their peaks are located at different magnitudes and their shapes also differ in declining and increasing slope.

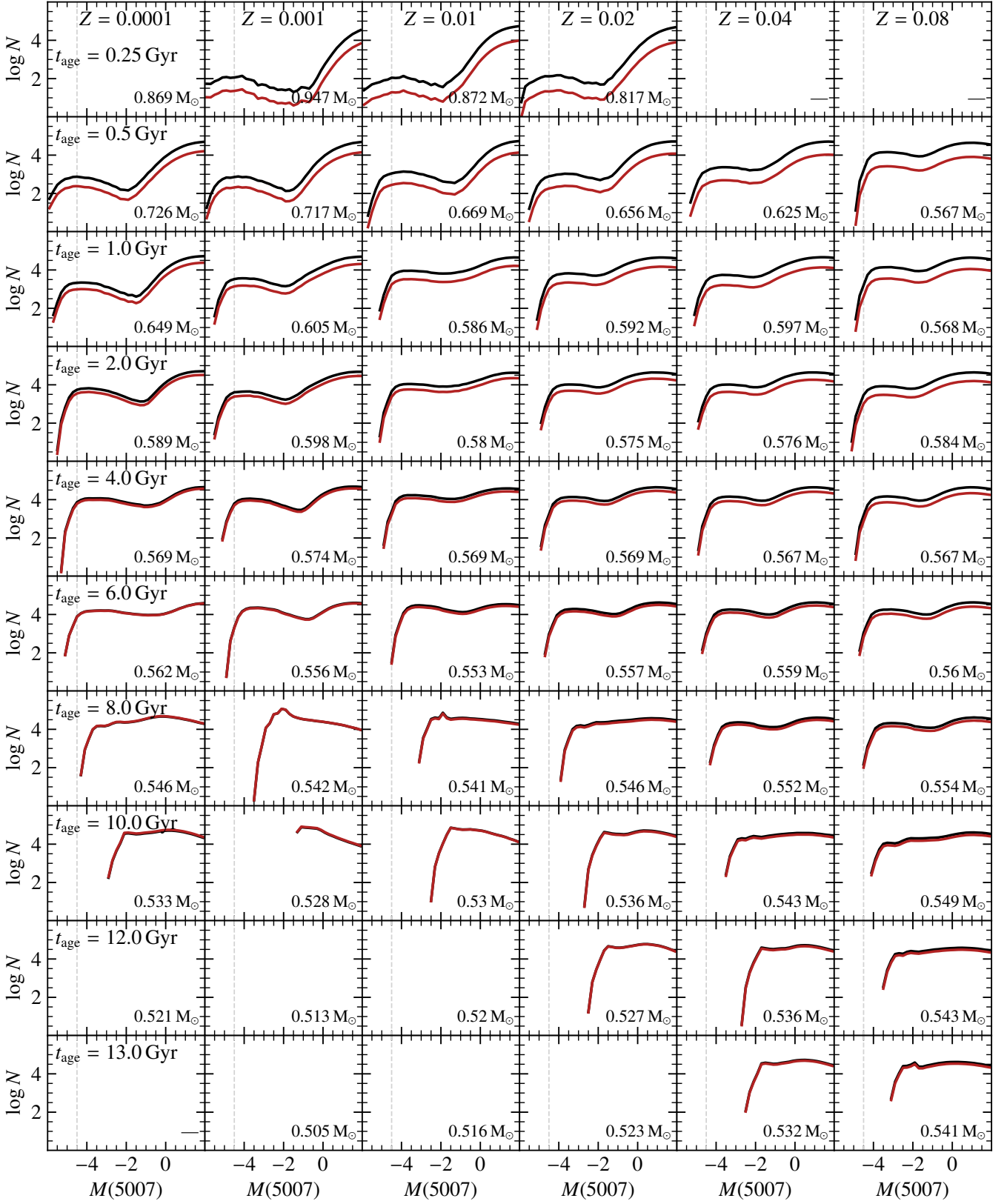


Fig. B.1. Single stellar population PNLFs depending on the age and metallicity for the fiducial model. This grid of PNLFs shows the same plots as seen in Fig. 7, except that the $\lambda 5007$ magnitude range is extended to dimmer PNe by four magnitudes. Rows correspond to the different ages and columns to the metallicities. The final masses resulting from the initial masses are computed from the IFMR of Miller Bertolami (2016) and are stated in the lower left corner of each panel. In the cases where the values lie outside the modeled range, only a dash is shown. The black lines are the PNLFs obtained from 10^6 stars of the respective final mass with equally spaced post-AGB ages between 0 and 30 000 yr. The red PNLFs are rescaled for a Chabrier IMF (Chabrier 2003), such that they can be compared relative to each other (i.e., the more massive stars are less frequent than lower-mass stars). The bright-end cutoff is marked by the vertical gray dashed line at $M(5007) = -4.5$.